RSC Advances

PAPER

View Article Online
View Journal | View Issue

Cite this: *RSC Adv.*, 2025, **15**, 26776

Precipitation synthesis and characterization of SnO_2@g-C_3N_4 heterojunctions for enhanced photocatalytic H_2 production†

Rizwan Khan,[ab] Shah Sawar Ahmad,[b] Hasnain Ihsan,[b] Syeda Sheeza Nadeem,[c] Syed Zulfiqar[b] and Ferry Anggoro Ardy Nugroho *[ad]

This study reports the development of SnO_2@g-C_3N_4 heterojunctions, a hybrid semiconductor photocatalyst with varying mass percent ratios using a facile precipitation method for hydrogen (H_2) production. The synergistic effect between the SnO_2 nanoparticles and g-C_3N_4 sheets suppresses the charge recombination and enhances carrier separation, leading to improved photocatalytic activity. The nanocomposites demonstrate increased hydrogen production across all composites, with SC-20 sample (*i.e.*, 80% SnO_2 and 20% g-C_3N_4) achieving the highest H_2 production rate of 287.7 μmol g^{-1} h^{-1}, that is, 1.87-fold and 1.63-fold higher than that of SnO_2 and of g-C_3N_4 counterparts, respectively. Furthermore, the nanocomposites maintain excellent photostability. Specifically, SC-20 achieves approximately 1500 μmol H_2 evolution per 5 hour-cycle. The facile precipitation-based synthesis and enhanced photocatalytic activity of the SnO_2@g-C_3N_4 nanocomposite position it as a reliable, cost-effective, and sustainable candidate for solar-driven hydrogen production and other clean energy applications.

Received 27th May 2025
Accepted 22nd July 2025

DOI: 10.1039/d5ra03721b

rsc.li/rsc-advances

Introduction

Population growth and rapid industrialization have significantly increased the global demand for energy, which is predominantly met by finite, non-renewable petroleum resources.[1–3] The continuous depletion of these energy reserves, combined with the environmental damage caused by their combustion, has accelerated global warming and climate change, creating an energy crisis that threatens both energy security and environmental sustainability.[4–8] To address these critical issues, relevant stakeholders have prioritized the development of alternative energy sources that are environmentally friendly, sustainable, and cost-effective. In this context, hydrogen energy has emerged as a promising solution to mitigate the energy crisis and to reduce environmental pollution due to its clean nature and high energy content.[9]

Prominent approaches to produce hydrogen include semiconductor-based photocatalytic water splitting. In particular, such a method has gained significant attention as a renewable and eco-friendly approach, as it not only provides a clean energy source but also reduces ecological pollution by decreasing reliance on fossil fuels.[10,11] Over the past few decades, various semiconductor materials explored for this purpose, specifically metal oxide materials including $SrTiO_3$, TiO_2, ZrO_2, Ta_2O_5, ZnO, WO_3, and SnO_2, have been systematically studied for their photocatalytic properties.[1,4,5,12–14] However, these materials face significant limitations. For instance, TiO_2 and SnO_2, with a large bandgap energy, absorb only UV light, utilizing merely 4% of sunlight. On the other hand, materials like ZnO are prone to photo-corrosion under illumination, while WO_3 is inactive for H_2 production due to its low conduction band edge potential.[13–15]

In response, several composite photocatalysts have been developed to address these limitations, among which graphitic carbon nitride (g-C_3N_4) emerged as a promising candidate.[16,17] g-C_3N_4 is a metal-free polymeric semiconductor with a suitable bandgap of 2.7 eV, enabling efficient sunlight absorption and charge carrier excitation.[18,19] Additionally, its high chemical and thermal stability, attributed to its polymeric structure and degree of polymerization, render it a robust material for photocatalytic applications.[20,21] Furthermore, g-C_3N_4 is cost-effective and can be readily synthesized through the simple thermal decomposition of urea.[22] As a result, it has been extensively explored for photocatalytic hydrogen evolution,[23,24] and a variety of g-C_3N_4-based heterostructures have been reported, including BiOCl/g-C_3N_4,[25] and CdS/g-C_3N_4,[26,27] and

[a]*Department of Physics, Faculty of Mathematics and Natural Sciences, Universitas Indonesia, Depok 16424, Indonesia. E-mail: f.a.a.nugroho@sci.ui.ac.id*
[b]*Department of Physics, Abdul Wali Khan University Mardan, Mardan, Pakistan*
[c]*Department of Chemistry, Faculty of Mathematics and Natural Sciences, Universitas Indonesia, Depok 16424, Indonesia*
[d]*Institute for Advanced Sustainable Materials Research and Technology, Faculty of Mathematics and Natural Sciences, Universitas Indonesia, Depok 16424, Indonesia*

† Electronic supplementary information (ESI) available. See DOI: https://doi.org/10.1039/d5ra03721b

metal oxide-based ones such as Bi_2WO_6/g-C_3N_4,[28,29] TiO_2/g-C_3N_4,[30,31] ZnO/g-C_3N_4,[32,33] and TaON/g-C_3N_4,[34] which have shown promise in suppressing charge recombination and enhancing photocatalytic performance through the formation of heterojunction.[35–39]

Among metal oxide-based heterostructures, tin dioxide (SnO_2) is notable due to its non-toxicity, low cost, and excellent optical, physical and photoelectrochemical properties,[40,41] which understandably finds wide range applications in, *e.g.*, energy storage, gas sensing, solar cells, photocatalysis, electronics, and electrochemical cells.[42–44] In the context of photocatalysts, previous studies have shown that SnO_2 outperforms ZnO and TiO_2 as an electron acceptor, making it a more appealing candidate for such a system.[45] With these properties, SnO_2 thus constitutes a rational choice to be coupled with g-C_3N_4 to enhance its photocatalytic performance.[46] In recent years, several studies have reported the synthesis of SnO_2/g-C_3N_4 heterostructures for photocatalytic hydrogen production using various methods, including ultrasonic-assisting deposition,[47] sol–gel,[48] hydrothermal,[49,50] and solid-phase methods.[51,52] While these techniques offer advantages like crystallinity, good interfacial contact, and promising H_2 evolution performance, they are often time consuming, require high temperature and pressure, and involve toxic solvents and specialized equipment, making them less scalable and environmentally friendly.[53] Therefore, developing simple, low-cost, scalable and eco-friendly techniques to synthesize SnO_2@g-C_3N_4 photocatalyst for hydrogen evolution is highly desirable.

As a response, in this study we report the successful synthesis of SnO_2@g-C_3N_4 hybrid photocatalyst *via* a simple and cost-effective precipitation method, which is widely recognized for producing metal oxide nanoparticles under mild conditions (ambient temperature and pressure) without the use of toxic gases.[54–57] To the best of our knowledge, no previous studies reported the use of precipitation-based synthesis for constructing SnO_2/g-C_3N_4 heterojunctions for photocatalytic H_2 production. To address this gap, we systematically varied the mass ratios of SnO_2 to g-C_3N_4, and we found SC-20 sample (*i.e.*, 80% SnO_2 and 20% g-C_3N_4) to deliver the highest and stable photocatalytic hydrogen production, indicating an optimal interface for charge transfer. Aided with various materials characterization, the improved hydrogen production is attributed to the enhancement in the photo-induced charge carrier separation and suppressed charge recombination. This performance positions our synthesis strategy to be comparable with other complex methods employing noble metal catalysts, highlighting its potential for further optimization and practical applications.

Experimental section

Chemicals

All chemicals, including urea (CH_4N_2O), $SnCl_2 \cdot 2H_2O$ and NH_3 were purchased from Sigma-Aldrich without further purification. DI water was produced using water distillation apparatus DU-L4 MEDILAB.

Synthesis of g-C_3N_4 nanosheets

g-C_3N_4 nanosheets were prepared using the bath sonication method. First, 10 g of urea (CH_4N_2O) was heated in a muffle furnace at 550 °C for 3 h to produce bulk g-C_3N_4, which was subsequently ground into a powder. To convert this into nanosheets, 0.05 g of g-C_3N_4 powder was sonicated in 50 mL of distilled water for 90 min. The material was washed seven times with distilled water and dried at 70 °C for 24 h, yielding the desired light-yellow g-C_3N_4 nanosheets.

Preparation of SnO_2 nanoparticles

SnO_2 nanoparticles were synthesized *via* precipitation. First, 2.5 g of $SnCl_2 \cdot 2H_2O$ was dissolved in 50 mL DI water under stirring. A diluted ammonia solution (4 mL of 35% ammonia in 26 mL DI water) was added dropwise under continuous stirring to the $SnCl_2 \cdot 2H_2O$ solution until the mixture turned milky at pH 9. The precipitate was washed five times with DI water by centrifugation, dried at 60 °C for 24 h, ground into a powder, and annealed at 400 °C for 2 h.

Preparation of SnO_2@g-C_3N_4 nanocomposites

SnO_2@g-C_3N_4 nanocomposites with varying mass ratios were synthesized *via* a precipitation method as illustrated in Fig. 1. Initially, a measured quantity of g-C_3N_4 was dispersed in DI water, followed by the dissolution of $SnCl_2 \cdot 2H_2O$ under continuous stirring. A 35% ammonia solution was added dropwise to the mixture under stirring until a milky precipitate formed at pH 9. The precipitate was washed five times with DI water, dried at 60 °C for 24 h, ground into a fine powder, and annealed at 400 °C for 2 h. The prepared composites were labeled as SC-X, where X denotes the at% of the g-C_3N_4, that is, SC-10 comprises 90% SnO_2 and 10% g-C_3N_4, SC-20 does 80% SnO_2 and 20% g-C_3N_4, SC-30 does 70% SnO_2 and 30% g-C_3N_4, and SC-40 does 60% SnO_2 and 40% g-C_3N_4.

Physiochemical characterizations

Various characterization techniques were employed to analyze the properties of the prepared samples. XRD (JDX-3532, JEOL) with Cu Kα radiation (λ = 1.5418 Å) at 40 kV and 30 mA confirmed the tetragonal structure for SnO_2, hexagonal structure for g-C_3N_4, and the coexistence of both in SnO_2@g-C_3N_4 composites. FTIR (Cary 630, Agilent Technologies) identified Sn–O and C–N vibrational modes in SnO_2 and g-C_3N_4, respectively. SEM (JSM-6490A, JEOL) revealed sheet-like morphology for g-C_3N_4, particle morphology for SnO_2, and heterojunction formation in the composites. UV-vis (PerkinElmer) spectra showed enhanced absorbance in the visible region for the composites. PL (LS45 PerkinElmer) investigated the lower recombination of photo-generated electrons.

Photoelectrochemical measurements

Photocurrent (PC) measurements and electrochemical impedance spectroscopy (EIS) were performed using a CHI-660E electrochemical workstation with platinum counter electrode,

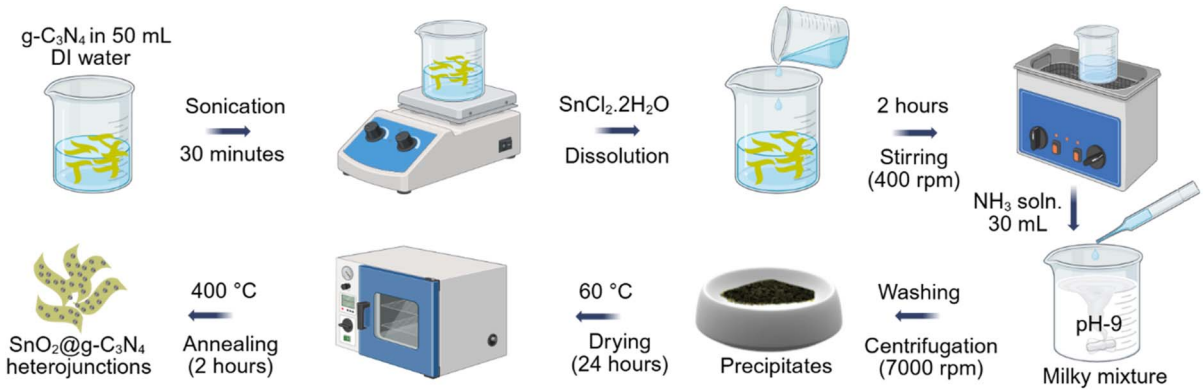

Fig. 1 Step-by-step schematic illustration of synthesis of SnO_2@g-C_3N_4 nanocomposites. First, the pre-synthesized g-C_3N_4 nanosheets are dispersed in 50 mL of deionized (DI) water. Subsequently, $SnCl_2 \cdot 2H_2O$ and NH_3 are added to the solution, followed by stirring and pH adjustment. After washing and drying, the resulting precipitates are then annealed. The final product, SnO_2@g-C_3N_4 composites, appears as light-yellow sheets with black dots on the surface.

Ag/AgCl reference electrode, and 0.5 M Na_2SO_4 electrolyte solution.

Photocatalytic H_2 generation measurements

Photocatalytic hydrogen production was evaluated in a flask irradiated by a 300 W xenon lamp (CEL HXF300), equipped with a cutoff filter ($\lambda > 420$ nm). For the experiment, 20 mg of the prepared sample was dispersed in 80 mL of aqueous solution containing 10% methanol as the hole scavenger, *via* ultrasonication. Prior to irradiation, the system was purged with nitrogen (N_2) for 15 min to eliminate any residual oxygen. The reaction was carried out under continuous stirring and illumination for a period of 5 h, and the amount of hydrogen produced was quantified using gas chromatography (GC-2014, Shimadzu).

Results and discussions

As the first step of our study, we investigate the structural properties and the molecular composition of our prepared samples using X-ray diffraction (XRD). Fig. 2a shows the obtained XRD patterns of pure g-C_3N_4 and SnO_2, their composites, as well as the corresponding JCPDS references for g-C_3N_4 and SnO_2. The diffraction pattern of pure g-C_3N_4 shows a characteristic peak at $2\theta = 27.5°$ corresponding to the (002) reflection of its graphitic stacking structure, which matches perfectly with the corresponding standard reference (ICSD 01-087-1526), confirming the hexagonal structure of pure g-C_3N_4.[58] In the case of pure SnO_2, observed peaks at 26.4°, 34°, 38°, 51.5°, and 65° correspond to (110), (101), (200), (211) and (301) planes, respectively, corroborating the tetragonal rutile structure of the SnO_2 (JCPDS 41-1445).[59] Examining the patterns of the composites (SC-10 to SC-40), the coexistence of both hexagonal g-C_3N_4 and tetragonal SnO_2 phases is confirmed, in that the corresponding patterns comprise the characteristic peaks of the constituents.[60] This finding thus corroborates the successful formation of heterojunction structures, notably without introducing any impurity phase. In detail, the intensity of the SnO_2 diffraction peaks gradually decrease with increasing g-C_3N_4 content from SC-10 to SC-30. Interestingly, among the composites, SC-40 shows a diffraction pattern closely resembling with pure g-C_3N_4, likely due to the higher g-C_3N_4 content in SC-40.

Moreover, FTIR spectroscopy was performed to analyze the chemical bonding and functional groups of the samples. As shown in Fig. 3, the pristine g-C_3N_4 exhibit peaks at 1243–1637 cm^{-1}, which correspond to C–N and C=N stretching vibrations, at 808 cm^{-1}, which is attributed to the tri-*s*-triazine ring structure, and at 3180–3331 cm^{-1}, which belongs to N–H stretching mode.[58,61] For pure SnO_2, a broad peak at 659 cm^{-1} represents the Sn–O stretching mode in Sn–O–Sn.[62] To this end, the absence of additional peaks in the spectra of pure g-C_3N_4 and SnO_2 confirms their high purity, consistent with the XRD data above. In the case of the composites (SC-10 to SC-30), the

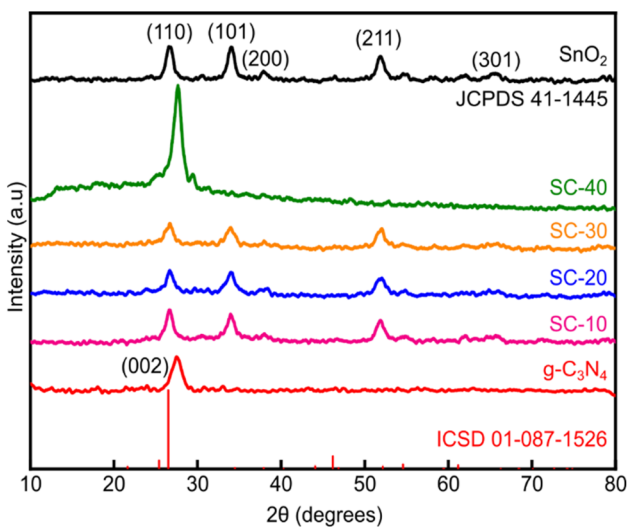

Fig. 2 X-ray diffraction pattern of g-C_3N_4, SnO_2, and their composites, alongside its standard reference. The coexistence of both g-C_3N_4 and SnO_2 signature peaks in the composite samples confirms their successful formation.

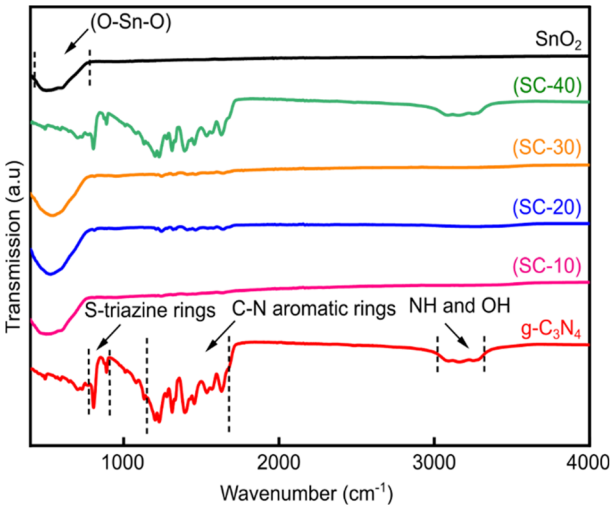

Fig. 3 FTIR spectra of pure g-C_3N_4, SnO_2, and their composites in the range of 500–4000 cm^{-1}. The characteristic C–N, C=N, and Sn–O bonds, along with some additional bonds, are observed in pure g-C_3N_4 and SnO_2, as well as their coexistence in the composites.

distinct vibrational modes of both g-C_3N_4 and SnO_2 are observed, corroborating the successful formation of the nanocomposites. The FTIR spectrum of SC-40, however, closely resembles that of g-C_3N_4, again indicating a dominant presence of g-C_3N_4 in this composition.

Last, Scanning Electron Microscopy (SEM) was employed to analyze the morphology of the synthesized samples. As shown in Fig. 4a and b, pure g-C_3N_4 exhibits a sheet-like morphology, though the sheets are not distinctly visible due to agglomeration. Meanwhile, Fig. 4c and d confirm the formation of well-defined SnO_2 nanoparticles with average diameters around 94.5 nm (Fig. S1†). When integrated into a heterostructure, the SnO_2 nanoparticles are expected to spread uniformly on the g-C_3N_4 sheets (Fig. 4e and f). In addition, energy dispersive X-ray (EDX) analysis confirmed the elemental composition and purity of g-C_3N_4, SnO_2 and SnO_2@g-C_3N_4 nanocomposite (Fig. S2†). Specifically, the g-C_3N_4 spectra displays distinct peaks corresponding to elements C and N, while SnO_2 shows peaks attributed to elements Sn and O. Finally, the SnO_2@g-C_3N_4 composite exhibits peaks Sn, O, C and N, confirming no impurity and creation of highly pure composite.

Next, we proceed to investigate the photoctalytic H_2 production performance of the synthesized heterostructures, along with those of their pure counterparts. To this end, we performed the photocatalytic reaction under visible light irradiation for 5 h (Fig. 5a). First we note that the hydrogen production of pure g-C_3N_4 is higher than that of SnO_2, throughout the reaction. Converting into production rate, pristine g-C_3N_4 exhibits H_2 production of 175.98 $\mu molg^{-1}$ h^{-1} compared to 160.84 $\mu molg^{-1}$ h^{-1} of SnO_2 (Fig. 5b). This behavior can be explained by the narrower bandgap, and thus higher visible light absorption, of g-C_3N_4 compared to SnO_2, as we will show later. Notably, and of our interest here, all four composites exhibit greater hydrogen generation than pure SnO_2 and g-C_3N_4, indicating the formation of an effective heterojunction that promotes interfacial charge transfer and suppresses photogenerated charge recombination. Among the composites, the champion sample is SC-20, whose production reaches 287.7 $\mu molg^{-1}$ h^{-1}, which is 1.63 times higher than g-C_3N_4 and 1.79 times higher than SnO_2. This performance enhancement can be attributed to the optimal ratio between SnO_2 and g-C_3N_4, which ensures sufficient interfacial contact for charge while maintaining visible light absorption. From the results in the composites it is evident that as the amount of SnO_2 increases, the hydrogen production increases, reaching a maximum at SC-20. Surprisingly, further increasing the SnO_2

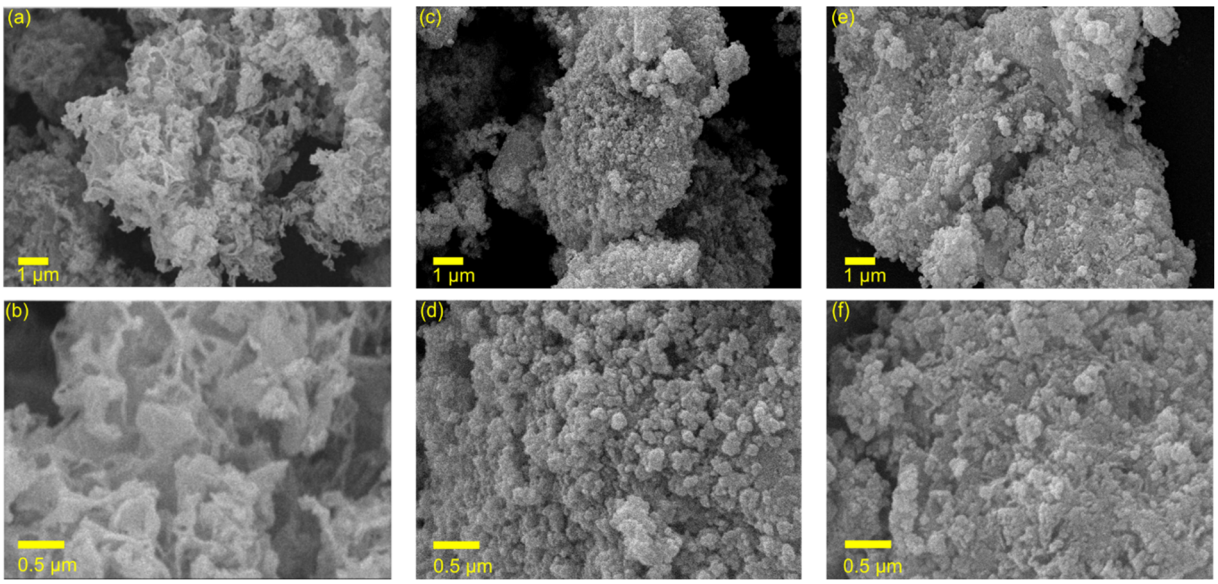

Fig. 4 Heterostructure morphology. SEM image of (a and b) g-C_3N_4, (c and d) SnO_2 and (e and f) SnO_2@g-C_3N_4 nanocomposites. g-C_3N_4 assumes sheet-like morphology, while SnO_2 does particle-like morphology. In the composite form, both these morphologies are observed.

content leads to a decline in hydrogen production at SC-10. This decline can be attributed to the shielding effect, as the g-C_3N_4 nanosheets become fully covered by SnO_2 nanoparticles. Since SnO_2 is a wide-bandgap semiconductor, this coverage inhibits the effective absorption of visible light, thereby reducing hydrogen production.[63,64] Furthermore, the hydrogen production level in SC-40 is comparable to that of pure g-C_3N_4, as the high g-C_3N_4 content dominates. This observation is consistent with the XRD pattern of the SC-40 above. Establishing that SC-20 outperforms all other composites, in the subsequent discussion we will focus on SC-20, alongside pure g-C_3N_4 and SnO_2 for further analysis regarding the enhancement mechanism.

To better understand the enhanced hydrogen evolution performance of SC-20 compared to its counterparts, additional verification of its optical properties is necessary. To assess the light-harvesting capabilities, UV-vis spectroscopy

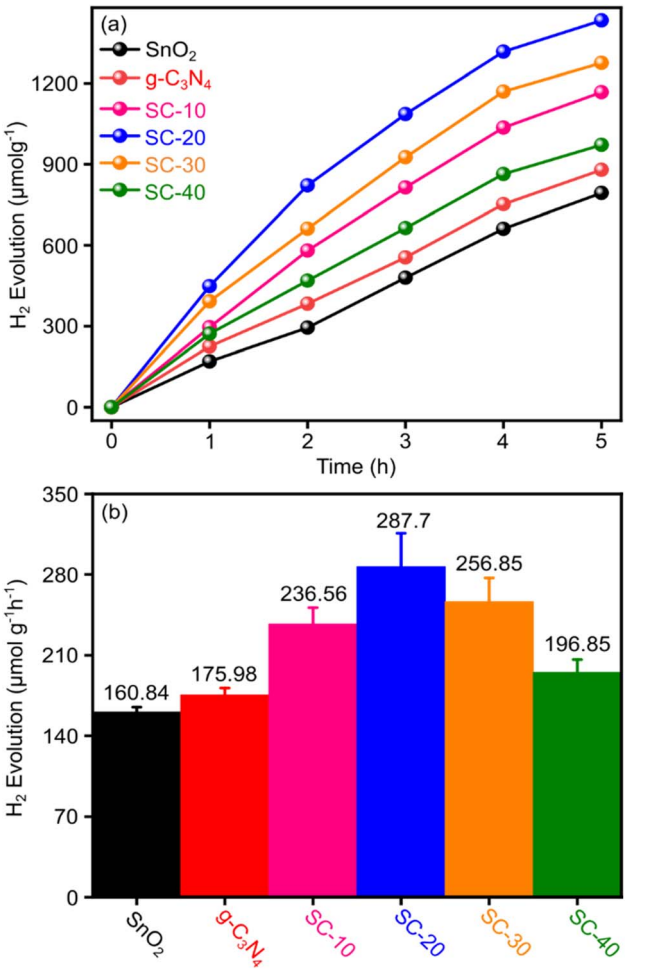

Fig. 5 Photocatalytic H_2 production performance of the as prepared SnO_2, g-C_3N_4, and their composites. (a) H_2 production over 5 h, showing SC-20 achieving the highest performance; (b) H_2 production rate per hour, where SC-20 outperforms pure SnO_2, g-C_3N_4, and other composites, a clear increasing trend is observed from SC-40 to SC-20, reaching a value of 287.7 $\mu molg^{-1}\ h^{-1}$. However, a further increase in SnO_2 content (SC-10) results in a decline in H_2 production, indicating SC-20 as the optimal composition.

was conducted in the wavelength range of 200–800 nm. The UV-vis spectra of pure SnO_2, g-C_3N_4, and SnO_2@g-C_3N_4 nanocomposites, along with their corresponding Tauc plots, are presented in Fig. 6a–d, respectively. Pure g-C_3N_4 shows strong absorption in the visible region due to its narrow bandgap (2.62 eV), while SnO_2 exhibit absorption predominantly in the UV region, attributed to its wider bandgap (3.29 eV). Notably, SC-20 sample demonstrates a broader absorption across both visible and UV regions. The Tauc plot of the composite SC-20 reveals an apparent bandgap of approximately 2.75 eV, which represents the integrated optical response of the heterostructure. This apparent bandgap likely arises from the synergistic interaction between SnO_2 and g-C_3N_4, leading to enhanced photoresponse and improved photocatalytic activity.[65,66]

Furthermore, to evaluate the separation efficiency and photoresponse of the photocatalysts, time-resolved photocurrent measurements were carried out under visible light illumination. In a photocurrent analysis, the sample is sandwiched between electrodes and then excited by a light pulse to generate charges. The photo-generated charges produce current on the electrodes, measured under light-on and light-off. The light-on phase represents charge buildup on electrodes, while light-off phase shows charge decay. As shown in Fig. 7a, SC-20 heterojunction exhibits the highest and most stable photocurrent density compared to pure SnO_2 and g-C_3N_4. The sharp photocurrent spikes under light-on and rapid decay during light-off indicate fast charge generation and relatively good carrier mobility. This enhanced photocurrent response in SC-20 can be attributed to improved charge separation and interfacial coupling between SnO_2 and g-C_3N_4, which facilitate directional charge transfer and reduce recombination losses. To further investigate charge transport dynamics, electrochemical impedance spectroscopy (EIS) was performed. In the Nyquist plots shown in Fig. 7b, SC-20 displays the smallest semicircular arc radius, indicating the lowest charge transfer resistance among the tested samples, followed by g-C_3N_4 and SnO_2. The decreased arc radius for SC-20 validates the formation of an efficient heterojunction, supporting the photocurrent findings. Moreover, photoluminescence (PL) spectroscopy was employed to assess photogenerated charge carrier recombination behavior in photocatalysts. In Fig. 7c SC-20 displayed significantly quenched photoluminescence intensity, compared to pure SnO_2 and g-C_3N_4. This quenching is the evidence of enhanced suppression of charge carrier recombination in the composite. These results collectively indicate that SC-20 heterostructure exhibits enhanced charge carrier separation, faster interfacial electron transport, and reduced recombination rates compared to the pure components.

Last, to evaluate the long-term photostability and practical viability of our SnO_2@g-C_3N_4 (SC-20) nanocomposite, a four-cycle photocatalytic hydrogen evolution test was conducted, with each cycle lasting 5 h under visible light irradiation (Fig. 8). Throughout all four cycles, the H_2 evolution rate remained nearly constant, suggesting excellent structural and photoelectrochemical stability. The consistent performance indicates

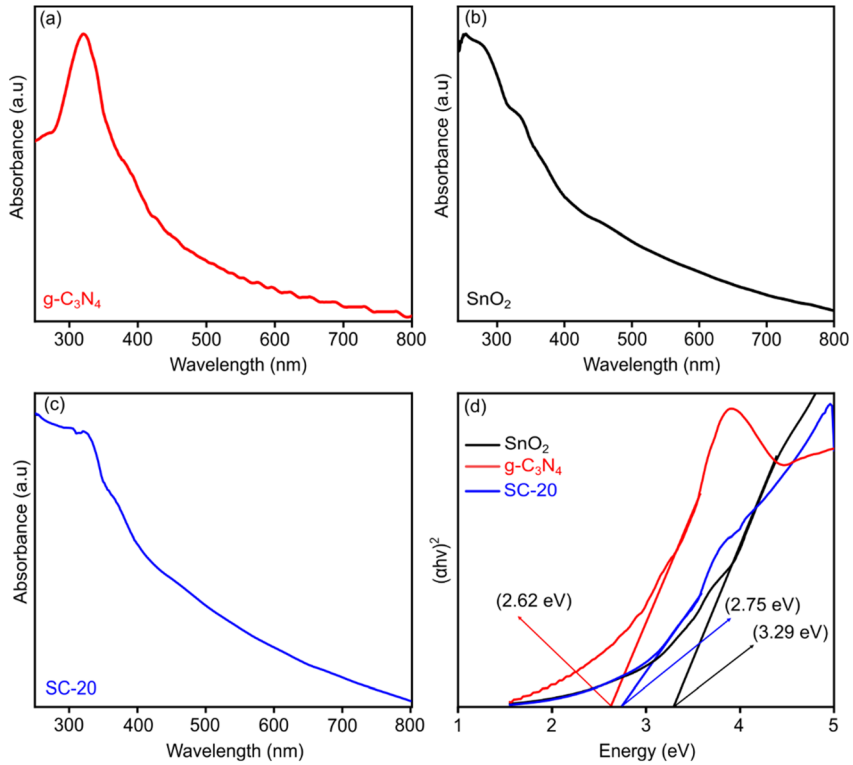

Fig. 6 Optical properties of g-C_3N_4, SnO_2, and SC-20 composite. UV-vis spectra of (a) g-C_3N_4, (b) SnO_2 and (c) SC-20 composite, along with their corresponding Tauc's plots shown as in (d). The band gaps were estimated to be 2.62 eV for g-C_3N_4, 3.29 eV for SnO_2, and 2.75 eV for SC-20. The slight increase in band gap of SC-20 compared to g-C_3N_4 is due to incorporation of SnO_2, while maintaining visible-light absorption, indicating successful heterojunction formation.

that the heterojunction interface effectively prevents photocorrosion and supports stable charge separation over extended illumination periods. Specifically, SC-20 achieves approximately 1500 μmol H_2 evolution per 5 hour-cycle, demonstrating negligible performance loss. This robustness surpasses that of many conventional such as TiO_2, ZnO, Fe_2O_3, and WO_3 based photocatalysts, which typically exhibit a noticeable decline in activity due to rapid charge accumulation, poor stability and limited visible light absorption.[67–70] The photocyclic results thus highlight the material's potential for real PEC applications requiring long-term operation without catalyst regeneration or replacement.

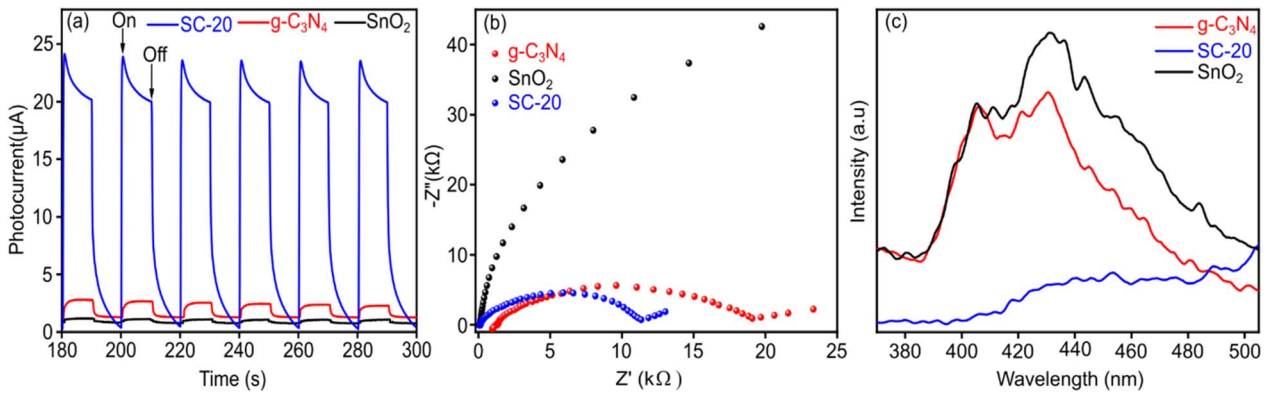

Fig. 7 Photocurrent, EIS, and PL analyses of SnO_2, g-C_3N_4, and SC-20. (a) Transient photocurrent response of pure SnO_2, g-C_3N_4, and SC-20 composite under chopped visible light irradiaion, shows that SC-20 exhibits a higher photocurrent compared to pure SnO_2 and g-C_3N_4, attributed to the synergistic effect in SC-20. (b) Nyquist plots of SC-20, g-C_3N_4, and SnO_2, illustrating their electrochemical impedance properties. SC-20 exhibits the smallest semi-circle, confirming the low charge transfer resistance in composite as compared to pure counterparts. (c) PL spectra of SC-20, g-C_3N_4, and SnO_2. SC-20 shows the lowest PL, indicating low charge recombination under illumination of visible light.

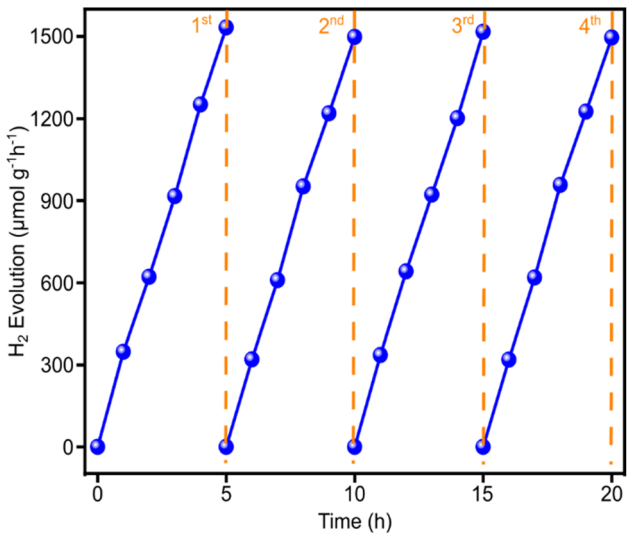

Fig. 8 Photostability of SC-20. Time-dependent H_2 evolution of SC-20 over four consecutive 5-hour cycles under visible light irradiation. Our best composite SC-20 maintains nearly constant H_2 production rate across all four cycles, demonstrating its strong photostability.

Comparative study

Having established the enhanced performance of our heterostructures compared to their pure counterparts, it is then interesting to benchmark them against other works reported in the literature employing similar heterostructures, however using different synthesis routes. As shown in Table 1, our composite, synthesized *via* a simple precipitation method, achieved a hydrogen evolution of 287.7 $\mu molg^{-1}$ h^{-1}, positioning it within the middle range of previously reported works. Notably, the heterostructures incorporating Pt as a co-catalyst or utilizing more advanced nanostructures such as quantum dots or nanodots have shown superior performance, often exceeding 1300 $\mu molg^{-1}$ h^{-1}. However, these methods often need precise control over nanostructures formation and multistep complicated synthesis methods, which can limit large-scale production. In conclusion, while advanced nanostructures and Pt incorporation boost H_2 evolution, our coprecipitation-based SnO_2@g-C_3N_4 nanocomposites offers a competitive balance of photocatalytic performance, synthesis simplicity, and cost-effectiveness. These findings suggest that further enhancements of photocatalytic activity may be possible through the incorporation of co-catalysts like Pt or quantum dots, as well as through refined interface engineering strategies.

Photocatalytic mechanism of SnO_2@g-C_3N_4

To close the discussion, a *Z*-scheme heterojunction mechanism is proposed based on band structure alignment and charge transfer behavior to explain the enhanced photocatalytic activity of SnO_2@g-C_3N_4 composite. As illustrated in Fig. 9, g-C_3N_4 is a visible light-driven photocatalyst with bandgap ≈ 2.62 eV (*cf.* Fig. 6d) while the photoresponse of SnO_2 is limited to UV-region with a bandgap ≈ 3.29 eV (*cf.* Fig. 6d). Furthermore, the conduction band position of g-C_3N_4 is (−1.12 eV *vs.* NHE) while SnO_2 have (0.05 eV *vs.* NHE).[78,79] upon solar illumination, both SnO_2 and g-C_3N_4 are excited to generate electron–hole pairs. In the *Z*-scheme configuration, photogenerated electrons in the conduction band of SnO_2 recombine with holes in the valence band of g-C_3N_4 at the heterojunction interface. This unique charge transfer pathway preserves the highly energetic electrons in the CB of g-C_3N_4 and the strong oxidizing holes in the VB of SnO_2, effectively enhancing the overall redox capability of the heterojunction.[60] As a result, the photogenerated electrons in the conduction band of g-C_3N_4 take participation in the reduction of H^+ ions to produce H_2. Meanwhile, photogenerated holes in the valence band of SnO_2 oxidize water molecules,

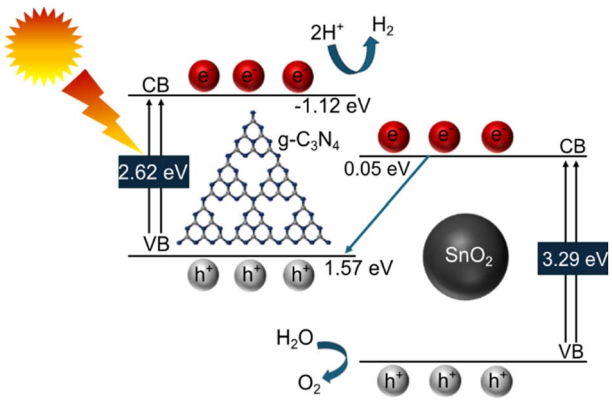

Fig. 9 Probable mechanism of the SnO_2@g-C_3N_4 photocatalyst: sunlight excites electrons in the valence band of g-C_3N_4, which transfer to the SnO_2 conduction band, driving the reduction of H^+ ions to H_2. Simultaneously, holes oxidize water to generate O_2. The diagram highlights the synergistic effect of combining SnO_2 and g-C_3N_4, to enhance photocatalytic performance.

Table 1 H_2 evolution performance of SnO_2/g-C_3N_4-based photocatalysts reported in the literature

Photocatalyst	Preparation method	Amount of H_2 gas evolved	References
g-C_3N_4/SnO_2	Solvent evaporation followed by calcination	132 μmol h^{-1}	71
Pt g^{-1}-C_3N_4/SnO_2	One pot pyrolysis	241 μmol h^{-1} g^{-1}	72
SnO_2@g-C_3N_4nanocomposites	**Coprecipitation**	**287.7 μmol $h^{-1}g^{-1}$**	**Our work**
Pt g^{-1}-C_3N_4/SnO_2	Simple calcination	627 μmol h^{-1}	73
g-C_3N_4/SnO_2–Pt	Physical mixing	900 μmol h^{-1} g^{-1}	74
C_3N_4–SnO_2–Pt	Hydrothermal	1060 μmol h^{-1} g^{-1}	75
SnO_2 QDs/g-C_3N_4	Thermal decomposition	1305.4 μmol h^{-1} g^{-1}	76
SnO_2 nanodots/g-C_3N_4	One-step polymerization	1398.2 μmol h^{-1} g^{-1}	77

generating O_2. The synergistic effect between these two components enhances overall photocatalytic performance. This mechanism aligns well with the experimental findings, including increased photocurrent response, reduced charge transfer resistance (EIS), and quenched PL intensity all of which confirm efficient charge separation and transport in the SnO_2@g-C_3N_4 heterostructure.

In addition to improved and charge carrier dynamics, the hydrogen adsorption on the catalyst surface is a critical factor influencing overall HER efficiency. Literature-based Gibbs free energy (ΔG_H*) studies provide further thermodynamic insight into this aspect. ΔG_H* is a key thermodynamic parameter for evaluating a material's catalytic activity toward the hydrogen evolution reaction (HER).[80] It reflects how favorably hydrogen atoms bind to the catalyst surface, which in turn governs the balance between adsorption and desorption steps. Ideally, an effective HER catalyst should have a ΔG_H* value close to zero, ensuring that hydrogen atoms can adsorb and desorb efficiently. If ΔG_H* is too positive, hydrogen adsorption is unfavorable, leading to sluggish HER kinetics. If it is too negative, hydrogen binds too strongly, hindering H_2 release.[81] For pristine g-C_3N_4, previous theoretical studies have reported a ΔG_H* value of approximately −0.54 eV, indicating relatively strong hydrogen binding and potentially slow desorption.[82] In contrast, SnO_2 surfaces have shown ΔG_H* values ranging from 0.85 eV to 2.37 eV at different crystallographic orientations and adsorption sites, suggesting unfavorable hydrogen adsorption that may limit the generation of active hydrogen intermediates.[83,84] Although the Gibbs free energy of hydrogen atom adsorption for the SnO_2@g-C_3N_4 heterojunction itself has not yet been theoretically investigated, the significantly improved experimental hydrogen evolution performance observed in this study and previously explored studies suggests that interfacial charge redistribution may help tune ΔG_H* closer to the thermoneutral range. This highlights the need for future theoretical studies to better understand the active sites and mechanisms of hydrogen adsorption in such heterostructures.

Conclusion

In summary, we have successfully synthesized SnO_2@g-C_3N_4 heterojunctions using a cost-effective and environmentally friendly precipitation method. Four composites with varying mass ratios of SnO_2 to g-C_3N_4 (SC-10, SC-20, SC-30, and SC-40) were prepared to evaluate their photocatalytic performance for hydrogen production under solar illumination. Among these, SC-20 (80% SnO_2, 20% g-C_3N_4) exhibited the best performance, achieving the highest H_2 production rate (287.7 $\mu molg^{-1}\ h^{-1}$) due to its optimal heterojunction structure, which effectively suppressed charge recombination and enhanced electron transfer to the conduction band. Compared to previously reported works, employing complex synthetic routes or noble metal co-catalysts, our approach offers a practical balance of photocatalytic efficiency, material simplicity, and stability. Importantly, the excellent photostability of our SnO_2@g-C_3N_4 composite, demonstrated over extended cycling, further reinforces the potential of this system for sustainable solar-to-fuel applications. Furthermore, this synthesis platform can be enhanced by introducing additional functional components such as Pt co-catalyst or nanostructure modifiers to further improve charge carrier dynamics and overall efficiency.

Data avaibility

All data generated or analyzed during this study are included in the article and its ESI.†

Author contributions

R. K.: investigation, formal analysis, data curation, validation, visualization, writing – original draft. S. S. A.: investigation. H. I.: investigation. S. S. N.: writing – original draft. S. Z.: conceptualization, data curation, methodology, validation, supervision, resources. F. A. A. N.: data curation, validation, supervision, resources, funding acquisition, writing – review and editing.

Conflicts of interest

The authors declare no conflict of interest.

Acknowledgements

We acknowledge funding by the Faculty of Mathematics and Natural Sciences, Universitas Indonesia, under Publication Grant scheme 2025.

References

1 A. Kumar, *et al.*, Recent progress in advanced strategies to enhance the photocatalytic performance of metal molybdates for H_2 production and CO_2 reduction, *J. Alloys Compd.*, 2024, **971**, 172665.
2 Y. Zheng, J. Liu, J. Liang, M. Jaroniec and S. Z. Qiao, Graphitic carbon nitride materials: controllable synthesis and applications in fuel cells and photocatalysis, *Energy Environ. Sci.*, 2012, **5**, 6717–6731.
3 S. Patial, *et al.*, Tunable photocatalytic activity of $SrTiO_3$ for water splitting: Strategies and future scenario, *J. Environ. Chem. Eng.*, 2020, **8**, 103791.
4 S. Hou, Y. Li, W. Li, X. Ma and Y. Fan, Novel noble-metal-free NiCo-LDH/CdSe S-type heterojunction with built-in electric field for high-efficiency photocatalytic H_2 production, *J. Taiwan Inst. Chem. Eng.*, 2024, **156**, 105394.
5 F. Liu, *et al.*, Vacancy engineering mediated hollow structured ZnO/ZnS S-scheme heterojunction for highly efficient photocatalytic H_2 production, *Chin. J. Catal.*, 2024, **64**, 152–165.
6 W. Shi, *et al.*, Construction of ZrC@ $ZnIn_2S_4$ core–shell heterostructures for boosted near-infrared-light driven photothermal-assisted photocatalytic H_2 evolution, *Chem. Eng. J.*, 2023, **474**, 145690.
7 J. Lu, *et al.*, Construction of S-scheme heterojunction catalytic nanoreactor for boosted photothermal-assisted

photocatalytic H_2 production, *Appl. Surf. Sci.*, 2024, **642**, 158648.
8 Z. Yan, *et al.*, Photocatalysis for synergistic water remediation and H_2 production: A review, *Chem. Eng. J.*, 2023, **472**, 145066.
9 S. V. P. Vattikuti, P. A. K. Reddy, J. Shim and C. Byon, Visible-Light-Driven Photocatalytic Activity of SnO_2-ZnO Quantum Dots Anchored on g-C_3N_4 Nanosheets for Photocatalytic Pollutant Degradation and H_2 Production, *ACS Omega*, 2018, **3**, 7587–7602.
10 M. R. Hoffmann, S. T. Martin, W. Choi and D. W. Bahnemann, Environmental Applications of Semiconductor Photocatalysts, *Chem. Rev.*, 1995, **95**, 69–96.
11 X. Chen, S. Shen, L. Guo and S. S. Mao, Semiconductor-based photocatalytic hydrogen generation, *Chem. Rev.*, 2010, **110**, 6503–6570.
12 R. Singh, Different anticipated criteria to achieve novel and efficient photocatalysis *via* green ZnO: scope and challenges, *Int. J. Environ. Sci. Technol.*, 2022, **19**, 9209–9242.
13 S. Martha, P. Chandra Sahoo and K. M. Parida, An overview on visible light responsive metal oxide based photocatalysts for hydrogen energy production, *RSC Adv.*, 2015, **5**, 61535–61553.
14 K. Mallikarjuna, G. A. K. M. Rafiqul Bari, S. V. P. Vattikuti and H. Kim, Synthesis of carbon-doped SnO_2 nanostructures for visible-light-driven photocatalytic hydrogen production from water splitting, *Int. J. Hydrogen Energy*, 2020, **45**, 32789–32796.
15 K. Hashimoto, H. Irie and A. Fujishima, TiO_2 photocatalysis: A historical overview and future prospects, *Jpn. J. Appl. Phys.*, 2005, **44**, 8269–8285.
16 L. Mao, *et al.*, Simultaneous bulk and surface modifications of g-C_3N_4 *via* supercritical CO_2-assisted post-treatment towards enhanced photocatalytic activity, *Appl. Catal. B Environ. Energy*, 2025, **362**, 124712.
17 D. Liu, *et al.*, Constructing asymmetric dual active sites of Ag single atoms and nitrogen defects on carbon nitride for enhanced photocatalytic H_2O_2 production, *J. Mater. Sci. Technol.*, 2025, **223**, 56–65.
18 T. Li, *et al.*, Synthesis of g-C_3N_4/$SmVO_4$ composite photocatalyst with improved visible light photocatalytic activities in RhB degradation, *Appl. Catal., B*, 2013, **129**, 255–263.
19 W. Iqbal, *et al.*, One-step large-scale highly active gC3N4 nanosheets for efficient sunlight-driven photocatalytic hydrogen production, *Dalton Trans.*, 2017, **46**, 10678.
20 G. Dong, Y. Zhang, Q. Pan and J. Qiu, A fantastic graphitic carbon nitride (g-C_3N_4) material: Electronic structure, photocatalytic and photoelectronic properties, *J. Photochem. Photobiol. C Photochem. Rev.*, 2014, **20**, 33–50.
21 I. Papailias, *et al.*, Chemical *vs.* thermal exfoliation of g-C_3N_4 for NO_x removal under visible light irradiation, *Appl. Catal., B*, 2018, **239**, 16–26.
22 Y. He, *et al.*, Z-scheme SnO_{2-x}/g-C_3N_4 composite as an efficient photocatalyst for dye degradation and photocatalytic CO_2 reduction, *Sol. Energy Mater. Sol. Cells*, 2015, **137**, 175–184.
23 A. Mishra, *et al.*, Graphitic carbon nitride (g–C_3N_4)–based metal-free photocatalysts for water splitting: A review, *Carbon*, 2019, **149**, 693–721.
24 Y. Zhu, D. Zhang, L. Gong, L. Zhang and Z. Xia, Catalytic activity origin and design principles of graphitic carbon nitride electrocatalysts for hydrogen evolution, *Front. Mater.*, 2019, **6**, 439322.
25 Y. Bai, P. Q. Wang, J. Y. Liu and X. J. Liu, Enhanced photocatalytic performance of direct Z-scheme BiOCl–g-C_3N_4 photocatalysts, *RSC Adv.*, 2014, **4**, 19456–19461.
26 J. Zhang, *et al.*, Efficient visible-light photocatalytic hydrogen evolution and enhanced photostability of core/shell CdS/g-C_3N_4 nanowires, *ACS Appl. Mater. Interfaces*, 2013, **5**, 10317–10324.
27 L. Ge, *et al.*, Synthesis and efficient visible light photocatalytic hydrogen evolution of Polymeric g-C_3N_4 coupled with CdS quantum dots, *J. Phys. Chem. C*, 2012, **116**, 13708–13714.
28 J. Wang, X. Lian, S. Chen, H. Li and K. Xu, Effect of Bi_2WO_6/g-C_3N_4 composite on the combustion and catalytic decomposition of energetic materials: An efficient catalyst with g-C_3N_4 carrier, *J. Colloid Interface Sci.*, 2022, **610**, 842–853.
29 S. Qi, R. Zhang, Y. Zhang, X. Liu and H. Xu, Preparation and photocatalytic properties of Bi2WO6/g-C_3N_4, *Inorg. Chem. Commun.*, 2021, **132**, 108761.
30 X. Du, X. Bai, L. Xu, L. Yang and P. Jin, Visible-light activation of persulfate by TiO_2/g-C_3N_4 photocatalyst toward efficient degradation of micropollutants, *Chem. Eng. J.*, 2020, **384**, 123245.
31 H. Yan and H. Yang, TiO_2–g-C_3N_4 composite materials for photocatalytic H_2 evolution under visible light irradiation, *J. Alloys Compd.*, 2011, **509**, 26–29.
32 Y. He, Y. Wang, L. Zhang, B. Teng and M. Fan, High-efficiency conversion of CO_2 to fuel over ZnO/g-C_3N_4 photocatalyst, *Appl. Catal., B*, 2015, **168–169**, 1–8.
33 W. Liu, M. Wang, C. Xu, S. Chen and X. Fu, Significantly enhanced visible-light photocatalytic activity of g-C_3N_4 *via* ZnO modification and the mechanism study, *J. Mol. Catal. A:Chem.*, 2013, **369**, 9–15.
34 S. C. Yan, S. B. Lv, Z. S. Li and Z. G. Zou, Organic-inorganic composite photocatalyst of g-C_3N_4 and TaON with improved visible light photocatalytic activities, *Dalton Trans.*, 2010, **39**, 1488–1491.
35 P. Mary Rajaitha, *et al.*, Graphitic carbon nitride nanoplatelets incorporated titania based type-II heterostructure and its enhanced performance in photoelectrocatalytic water splitting, *Appl. Sci.*, 2020, **2**, 572.
36 M. Ramachandra, S. Devi Kalathiparambil Rajendra Pai, J. Resnik Jaleel UC and D. Pinheiro, Improved Photocatalytic Activity of g-C_3N_4/ZnO: A Potential Direct Z-Scheme Nanocomposite, *ChemistrySelect*, 2020, **5**, 11986–11995.
37 D. Li, *et al.*, Synthesis of a g-C_3N_4-Cu_2O heterojunction with enhanced visible light photocatalytic activity by PEG, *J. Colloid Interface Sci.*, 2018, **531**, 28–36.

38 T. Zhang, *et al.*, A facile one-pot and alkali-free synthetic procedure for binary SnO_2/g-C_3N_4 composites with enhanced photocatalytic behavior, *Mater. Sci. Semicond. Process.*, 2020, **115**, 105112.

39 A. R. Fareza, F. A. A. Nugroho, F. F. Abdi and V. Fauzia, Nanoscale metal oxides–2D materials heterostructures for photoelectrochemical water splitting—a review, *J. Mater. Chem. A*, 2022, **10**, 8656–8686.

40 H. Wang and A. L. Rogach, Hierarchical SnO_2 nanostructures: Recent advances in design, synthesis, and applications, *Chem. Mater.*, 2014, **26**, 123–133.

41 Y. Li, *et al.*, Rapid fabrication of SnO_2 nanoparticle photocatalyst: computational understanding and photocatalytic degradation of organic dye, *Inorg. Chem. Front.*, 2018, **5**, 3005–3014.

42 B. Xiong Wen Lou, C. Ming Li and L. A. Archer, Designed Synthesis of coaxial SnO_2@ carbon hollow nanospheres for highly reversible lithium storage, *Adv. Mater.*, 2009, **21**, 2536–2539.

43 J. Pan, R. Ganesan, H. Shen and S. Mathur, Plasma-modified SnO_2 nanowires for enhanced gas sensing, *J. Phys. Chem. C*, 2010, **114**, 8245–8250.

44 J. Pan, *et al.*, Heteroepitaxy of SnO_2 nanowire arrays on TiO_2 single crystals: Growth patterns and tomographic studies, *J. Phys. Chem. C*, 2011, **115**, 15191–15197.

45 M. T. Uddin, *et al.*, Nanostructured SnO_2-ZnO heterojunction photocatalysts showing enhanced photocatalytic activity for the degradation of organic dyes, *Inorg. Chem.*, 2012, **51**, 7764–7773.

46 K. N. Van, *et al.*, Facile construction of S-scheme SnO2/g-C_3N_4 photocatalyst for improved photoactivity, *Chemosphere*, 2022, **289**, 133120.

47 R. Yin, *et al.*, SnO_2/g-C_3N_4 photocatalyst with enhanced visible-light photocatalytic activity, *J. Mater. Sci.*, 2014, **49**, 6067–6073.

48 L. Peng, R. rong Zheng, D. wei Feng, H. Yu and X. ting. Dong, Synthesis of eco-friendly porous g-C_3N_4/SiO_2/SnO_2 composite with excellent visible-light responsive photocatalysis, *Arab. J. Chem.*, 2020, **13**, 4275–4285.

49 Y. Zhang, J. Liu, X. Chu, S. Liang and L. Kong, Preparation of g–C_3N_4–SnO_2 composites for application as acetic acid sensor, *J. Alloys Compd.*, 2020, **832**, 153355.

50 K. N. Van, *et al.*, Facile construction of S-scheme SnO_2/g-C_3N_4 photocatalyst for improved photoactivity, *Chemosphere*, 2022, **289**, 133120.

51 Y. He, *et al.*, Z-scheme SnO_{2-x}/g-C_3N_4 composite as an efficient photocatalyst for dye degradation and photocatalytic CO_2 reduction, *Sol. Energy Mater. Sol. Cells*, 2015, **137**, 175–184.

52 X. Wang and P. Ren, Flower-like SnO_2/g-C_3N_4 heterojunctions: The face-to-face contact interface and improved photocatalytic properties, *Adv. Powder Technol.*, 2018, **29**, 1153–1157.

53 W. Ren, *et al.*, Recent progress in SnO_2/g-C_3N_4 heterojunction photocatalysts: Synthesis, modification, and application, *J. Alloys Compd.*, 2022, **906**, 164372.

54 A. K. Atul, S. K. Srivastava, A. K. Gupta and N. Srivastava, Synthesis and characterization of NiO nanoparticles by chemical co-precipitation method: an easy and cost-effective approach, *Braz. J. Phys.*, 2022, **52**, 2.

55 M. J. Ndolomingo, N. Bingwa and R. Meijboom, Review of supported metal nanoparticles: synthesis methodologies, advantages and application as catalysts, *J. Mater. Sci.*, 2020, **55**, 6195–6241.

56 G. N. Kokila, C. Mallikarjunaswamy and V. L. Ranganatha, A review on synthesis and applications of versatile nanomaterials, *Inorg. Nano-Met. Chem.*, 2022, **54**, 942–971.

57 M. Aminzai, M. Yildirim and E. Y. Talanta, Metallic nanoparticles unveiled: Synthesis, characterization, and their environmental, medicinal, and agricultural applications, *Talanta*, 2024, **280**, 126790.

58 P. Agale, V. Salve, S. Arade, S. Balgude and P. More, Tailoring structural and chemical properties of ZnO@ g-C_3N_4 nanocomposites through Sr doping: Insights from multi technique characterization, *Solid State Sci.*, 2025, **166**, 107960.

59 J. Cao, *et al.*, Calcination Method Synthesis of SnO_2/g-C_3N_4 Composites for a High-Performance Ethanol Gas Sensing Application, *Nanomaterials*, 2017, **7**, 98.

60 V. Salve, *et al.*, Enhanced photocatalytic activity of SnO_2@g-C_3N_4 heterojunctions for methylene blue and bisphenol-A degradation: effect of interface structure and porous nature, *RSC Adv.*, 2025, **15**, 15651–15669.

61 L. Mao, *et al.*, Simultaneous bulk and surface modifications of g-C_3N_4 *via* supercritical CO_2-assisted post-treatment towards enhanced photocatalytic activity, *Appl. Catal. B Environ. Energy*, 2025, **362**, 124712.

62 Y. Zang, L. Li, X. Li, R. Lin and G. Li, Synergistic collaboration of g-C_3N_4/SnO_2 composites for enhanced visible-light photocatalytic activity, *Chem. Eng. J.*, 2014, **246**, 277–286.

63 H. Wu, *et al.*, A facile one-step strategy to construct 0D/2D SnO_2/g-C_3N_4 heterojunction photocatalyst for high-efficiency hydrogen production performance from water splitting, *Int. J. Hydrogen Energy*, 2020, **45**, 30142–30152.

64 A. Zada, M. Khan, M. N. Qureshi, S. Y. Liu and R. Wang, Accelerating Photocatalytic Hydrogen Production and Pollutant Degradation by Functionalizing g-C_3N_4 With SnO_2, *Front. Chem.*, 2020, **7**, 941.

65 Y. Zang, L. Li, X. Li, R. Lin and G. Li, Synergistic collaboration of g-C_3N_4/SnO_2 composites for enhanced visible-light photocatalytic activity, *Chem. Eng. J.*, 2014, **246**, 277–286.

66 H. Ji, *et al.*, Construction of SnO_2/graphene-like g-C_3N_4 with enhanced visible light photocatalytic activity, *RSC Adv.*, 2017, **7**, 36101–36111.

67 H. Khan and M. U. H. Shah, Modification strategies of TiO_2 based photocatalysts for enhanced visible light activity and energy storage ability: A review, *J. Environ. Chem. Eng.*, 2023, **11**, 111532.

68 K. Hasibur Rahman, A. Kumar Kar and K. C. Chen, Highly active ZnO/Fe_3+-TiO_2 photocatalysts for visible-light photodegradation application and its colour change

behaviour by d-d transition, *Mater. Sci. Eng., B*, 2024, **305**, 117394.

69 Q. Wang, *et al.*, Hollow spherical WO_3/TiO_2 heterojunction for enhancing photocatalytic performance in visible-light, *J. Water Proc. Eng.*, 2021, **40**, 101943.

70 A. Raub, R. Bahru and S. Nashruddin, Advances of nanostructured metal oxide as photoanode in photoelectrochemical (PEC) water splitting application, *Heliyon*, 2024, **10**, e39079.

71 A. Zada, M. Khan, M. N. Qureshi, S. Liu and R. Wang, Accelerating Photocatalytic Hydrogen Production and Pollutant Degradation by Functionalizing g-C_3N_4 With SnO_2, *Front. Chem.*, 2020, **7**, 941.

72 C. Cai, *et al.*, Facile one-pot pyrolysis preparation of SnO_2/g-C_3N_4 composites for improved photocatalytic H2 production, *J. Chem. Technol. Biotechnol.*, 2022, **97**, 2921–2931.

73 M. Ismael, E. Elhaddad and M. Wark, Construction of SnO_2/g-C_3N_4 composite photocatalyst with enhanced interfacial charge separation and high efficiency for hydrogen production and Rhodamine B degradation, *Colloids Surf. A Physicochem. Eng. Asp.*, 2022, **638**, 128288.

74 Y. Zang, L. Li, X. Li, R. Lin and G. Li, Synergistic collaboration of g-C_3N_4/SnO_2 composites for enhanced visible-light photocatalytic activity, *Chem. Eng. J.*, 2014, **246**, 277–286.

75 X. Wang, M. Xue, X. Li, L. Qin and S.-Z. Kang, Boosting the photocatalytic H_2 production performance and stability of C_3N_4 nanosheets *via* the synergistic effect between SnO_2 nanoparticles and Pt nanoclusters, *Inorg. Chem. Commun.*, 2021, **133**, 108976.

76 S. V. P. Vattikuti, H. P. K. Sudhani, M. A. Habila, P. Rosaiah and J. Shim, SnO_2 Quantum Dot-Decorated g-C_3N_4 Ultrathin Nanosheets: A Dual-Function Photocatalyst for Pollutant Degradation and Hydrogen Evolution, *Catalysts*, 2024, **14**, 824.

77 H. Wu, *et al.*, A facile one-step strategy to construct 0D/2D SnO_2/g-C_3N_4 heterojunction photocatalyst for high-efficiency hydrogen production performance from water splitting, *Int. J. Hydrogen Energy*, 2020, **45**, 30142–30152.

78 A. Seza, *et al.*, Novel microwave-assisted synthesis of porous g-C_3N_4/SnO_2 nanocomposite for solar water-splitting, *Appl. Surf. Sci.*, 2018, **440**, 153–161.

79 K. Zhu, *et al.*, Facile fabrication of g-C_3N_4/SnO_2 composites and ball milling treatment for enhanced photocatalytic performance, *J. Alloys Compd.*, 2019, **802**, 13–18.

80 J. K. Nørskov, *et al.*, Trends in the Exchange Current for Hydrogen Evolution, *J. Electrochem. Soc.*, 2005, **152**, J23.

81 N. T. Suen, *et al.*, Electrocatalysis for the oxygen evolution reaction: recent development and future perspectives, *Chem. Soc. Rev.*, 2017, **46**, 337–365.

82 Y. Zheng, *et al.*, Hydrogen evolution by a metal-free electrocatalyst, *Nat. Commun.*, 2014, **5**, 3783.

83 E. German, C. Pistonesi and V. Verdinelli, A DFT study of H_2 adsorption on Pdn/SnO_2 (110) surfaces ($n = 1$–10), *Eur. Phys. J. B*, 2019, **92**, 98.

84 R. B. Goncalves, Z. Chen, K. W. Chapman, R. Q. Snurr and J. T. Hupp, Experimental and theoretical investigation of hydrogen sorption by SnO_2 nanostructures in a metal–organic framework scaffold, *Mol. Phys.*, 2025, e2499204.